



Dislocation-enhanced electrical conductivity in rutile TiO₂ accessed by room-temperature nanoindentation



Hanna Bishara^{a,*}, Hanna Tsybenko^a, Supriya Nandy^a, Qaisar Khushi Muhammad^b, Till Frömling^b, Xufei Fang^b, James P. Best^a, Gerhard Dehm^{a,*}

^a Max-Planck-Institut für Eisenforschung GmbH, Max-Planck-Str. 1, Düsseldorf 40237, Germany

^b Division of Nonmetallic-Inorganic Materials, Department of Materials and Earth Sciences, Technical University of Darmstadt, Darmstadt 64287, Germany

ARTICLE INFO

Article history:

Received 17 November 2021

Revised 17 January 2022

Accepted 17 January 2022

Keywords:

Dislocations

Titanium dioxide

Mechanical doping

Electrical conductivity

Impedance spectroscopy

ABSTRACT

Dislocation-enhanced electrical conductivity is an emerging topic for ceramic oxides. In contrast to the majority of present studies which focus on large-scale crystal deformation or thin film fabrication to introduce dislocations, we use a nanoindentation “pop-in stop” method to locally generate (011) edge-type dislocations at room temperature, without crack formation, on the (100) surface of a rutile TiO₂ single-crystal. Ion beam assisted deposition of microcontacts allowed for both deformed and non-deformed zones to be locally probed by impedance spectroscopy. Compared to the dislocation-free region, a local enhancement of the electrical conductivity by 50% in the dislocation-rich regions is found. The study paves the way for local “mechanical-doping” of ceramics and oxide materials, allowing for the use of dislocations to tune the local conductivity with high spatial resolution.

© 2022 The Author(s). Published by Elsevier Ltd on behalf of Acta Materialia Inc.

This is an open access article under the CC BY-NC-ND license

(<http://creativecommons.org/licenses/by-nc-nd/4.0/>)

Introducing dislocations into oxide ceramic materials via plastic deformation has been shown to improve the electrical conductivity [1–7]. Such modification of the electrical properties holds a high significance in energy applications, e.g., photovoltaics, electrochemistry, and battery technologies [8–10]. Despite the brittle nature of ceramics, dislocations can be introduced into the materials either by high-temperature compression [1,5], by controlling the sintering process [11], via bi-crystal bonding techniques [6], or other methods [8]. All techniques involve bulk-scale structural modification, which alters the properties of the whole crystal. In this work, we present a near surface-localised conductivity increase without affecting the surrounding bulk crystal structure through confined deformation of a rutile (TiO₂) single crystal using nanoindentation pop-in stop tests. The study paves the road for nanoscale spatial control of electrical properties in ionic solids, for instance, in developing printing-like technology to create local conductive paths of a micrometer dimensions within a ceramic material.

These distinct electronic characteristics of plastically deformed TiO₂ originate from the physical and chemical nature of dislocations. It has been shown that the Ti inside the dislocation core exhibits a mixed-valence state, which leads to a higher density of states at the Fermi level, and consequently increases the conduc-

tivity of the material [12]. In addition, impurities present in the material (e.g., induced by chemical reduction) significantly affect the conductivity of the bulk material and dislocations, as observed by conductive atomic force microscopy [13,14]. However, not only the dislocation core affects conductivity, but also, the overlapping space charge at the dislocation yields an increase in conductivity for dislocations spaced within tens of nanometers [5,15]. Therefore, the formation of highly dense dislocation arrays are promising for enhanced material conductivity.

Tetragonal TiO₂ is known to plastically deform under bulk compression only when $T \geq 600$ °C [16–18], where the active slip systems observed are $\{101\} \langle 10\bar{1} \rangle$ and $\{100\} \langle 0\bar{1}0 \rangle$. $\langle 10\bar{1} \rangle$ dislocations dissociate into two partials to form stacking faults due to their low stacking fault energy [11,16,17,19,20]. Dislocations on the $\{100\}$ slip planes, on the other hand, tend not to dissociate [20,21]. In contrast to bulk compression, the room temperature plasticity of TiO₂ has been demonstrated using nanoindentation [22–27]. The indentation of the (100) surface yields activation of the aforementioned slip systems, with no observable competition [23]. Among these studies, only stacking fault formation has been observed without discussion on the origin of the phenomena and rigorous slip system analysis. Moreover, the brittleness of TiO₂ at room temperature results in crack formation, which only a few studies have circumvented by using extremely low load during nanoindentation [26,27].

* Corresponding authors.

E-mail addresses: h.bishara@mpie.de (H. Bishara), g.dehm@mpie.de (G. Dehm).

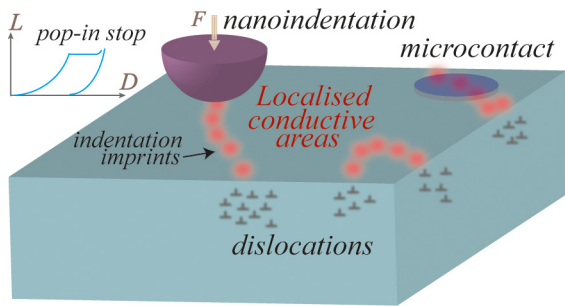


Fig. 1. Schematic for the creation of local conductive areas (dislocation-rich) within an oxide ceramic. The conductive areas are formed of shallow nanoindentation imprints, performed in a controlled manner to create a crack-free plastic zone. Microcontacts are employed to probe the local conductivity.

To achieve room temperature indentation-induced plastic deformation without crack formation in a ceramic material, nanoindentation must be performed in a well-controlled manner [28–32]. In this work, this has been achieved when loading is stopped after the first (or first few) pop-in events with an indenter with a small tip radius to reduce the probability of probing pre-existing flaws within the stressed indentation volume. As such, the generated shear stresses reach the resolved shear stress for dislocation activation before the fracture strength of the material. In addition, stopping the indentation loading profile shortly after the first pop-in ensures minimal plastic deformation with low interaction between the newly activated defects and indentation-induced stress field to suppress crack formation. This phenomenon is described in detail in Ref. [32].

In this paper, a local conductivity improvement of 50% was achieved using mechanical deformation of sub-micron volumes at the crystal surface. Shallow nanoindentation is performed on a TiO₂ single crystal, and the resulting initial dislocation plasticity analysed. Local impedance measurements were then performed on both the deformed and non-deformed regions via microcontacts deposited over nanoindentation arrays, as illustrated in Fig. 1.

Indentation experiments were conducted on the (100) polished surface of the as-received rutile TiO₂ sample (CrysTech GmbH, Germany) using a KLA (Agilent, Keysight, USA) G200 nanoindenter. The surface was indented with a spherical diamond tip with a nominal tip radius of 1 μm under a constant strain rate of 0.05 s⁻¹ until a target penetration depth was reached. To identify the target indentation depth, a single pre-test was performed to a maximum depth of 100 nm. During the pre-test, the first pop-in event occurred at a load of ~1.3 mN and penetration depth of ~35 nm. Therefore, to ensure the occurrence of the first pop-in event, the indentation experiments were carried out to a target depth of 55 nm. To show that the phenomenon does not depend on the indenter shape, a similar procedure was performed using a diamond Berkovich indentation tip (Synton MDP, Switzerland).

The load-displacement characteristics were distinct for the spherical and Berkovich indenter tip geometries used; a representative indentation curve for each indenter type is presented in Fig. 2a. Loading was removed shortly after the pop-in and, as such, each indent showed a single pop-in event corresponding to dislocation activity, as evidenced later. The spherical and Berkovich indentation curves follow a Hertzian response up to the pop-in event. The pop-in loads and displacements additionally depend on the indenter geometry; Fig. 2b reveals higher pop-in loads for indentation with a spherical indenter compared to the Berkovich indenter due to the larger contact area of the spherical tip.

The deformation zones were characterised by controlled electron channeling contrast imaging (ECCI), using a beam current of 2 nA, an accelerating voltage of 30 kV, and a working distance of

~7 mm, in a scanning electron microscope (SEM, Zeiss Gemini-2). For both indenter geometries, the same slip systems were activated as identified using ECCI. Using the electron channeling pattern (ECP) and TOCA v2.3 (courtesy to S. Zaeferrer), EBSD Kikuchi patterns were indexed to simulate the ECPs. Simulated ECPs helped us to evaluate exact tilting conditions for defect observation under a predetermined diffraction vector (\vec{g}). Fig. 3a shows the traces of Berkovich indents for pop-in stop experiments, with dislocations forming in the $\langle 001 \rangle$ directions, while no dislocations are observed along the $\langle 010 \rangle$ direction. In case that indentation continues beyond the first pop-in event, cracks start to form, as shown in Fig. 3b. A similar trend is observed for the dislocation structure of the spherical indentation experiment (Fig. 3c–g).

The Burgers vector \vec{b} direction of these dislocations were characterized using $\vec{g}\vec{b} = 0$ analyses. The $\vec{g}\vec{b} = 0$ analyses for chosen \vec{g} vectors and possible Burgers vectors \vec{b} are shown in Table S1. According to this, dislocations with \vec{b} in $\langle 100 \rangle$ and $\langle 110 \rangle$ directions must be invisible under $\vec{g} = (001)$. This is, however, not the case, as shown in Fig. 3c. Therefore, the dislocations do not have \vec{b} in $\langle 100 \rangle$ and $\langle 110 \rangle$ directions. As the dislocations are invisible under $\vec{g} = (100)$ (Fig. 3d), these dislocations must be either $[011]$ and/or $[0\bar{1}1]$ and/or $[001]$. Further, these dislocations are invisible under $\vec{g} = (1\bar{1}1)$ (Fig. 3g); this observation reveals that the \vec{b} vector of these dislocations is $[011]$. Next, one can note that the dislocation line vectors are perpendicular to the obtained \vec{b} vector (as shown with the yellow arrow in Fig. 3a). This observation leads to the fact that these dislocations are edge type; such dislocations have been reported to be conductive [5].

The incipient plastic deformation observed for shallow nanoindentation of (100) TiO₂ at room temperature shows crack-free plasticity initiated at the pop-in event for a small enough indenter tip radius. The elastic modulus in the $[100]$ direction is calculated as 174 ± 7 GPa, based on the Hertzian fit of spherical indents before yielding. The measured modulus falls between a theoretically calculated value of ~147 GPa [33] and an experimentally reported value of ~229 GPa [23]. Berkovich indentation also follows a Hertzian response, with an effective tip radius of 400 nm. The maximum resolved shear stress to activate dislocation plasticity is calculated beneath the spherical indenter at the pop-in event [34]:

$$\tau_{\max} = 0.31 \left(\frac{6E_r^2}{\pi^3 r^2} P_0 \right)^{1/3} \quad (1)$$

where E_r is the reduced modulus which considers the elastic properties of the sample and indenter material [35]. E of 174 GPa is used from our spherical indentation measurement, while a Poisson's ratio (ν) of 0.25 was used [23]. An E of 1140 GPa and ν of 0.07 were used for the diamond tip [35]. Here, P_0 is the pop-in load, and r is the radius of the indenter tip, measured as 1 μm for the spherical indenter and calculated as 400 nm for the Berkovich indenter. Substitution of the pop-in loads presented in Fig. 2b into Eq. (1) indicates that plasticity is initiated at 5.9 ± 0.1 GPa and 7.5 ± 0.2 GPa for spherical and Berkovich indenters, respectively. τ_{\max} for the spherical indentation experiments is lower compared to the Berkovich result. This trend confirms the pop-in size effect [36], in which the larger spherical tip radius has a higher probability for probing pre-existing flaws and surface imperfections during the elastic contact prior to pop-in, and hence the pop-in stress is decreased.

The maximum resolved shear stress value for spherical indentation of the same crystallographic plane in TiO₂ was reported as 8.7 GPa [23]. Such differences in τ_{\max} are attributed to crystal quality variation and small variabilities in surface preparation which may affect the local stress state and dislocation nucleation at low contact depths [37]. Nevertheless, the dislocation density of the pristine sample is 2.5×10^4 dislocations per cm², corresponding

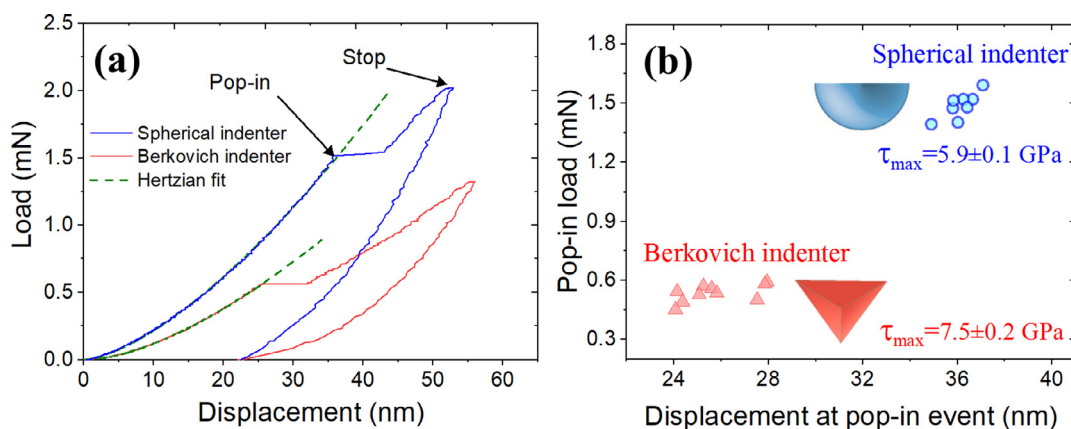


Fig. 2. Representative pop-in-stop indentation curves for spherical and Berkovich indenter geometries (a). The indentation curves follow a classic Hertzian elastic response until the pop-in event. Pop-in data scatter (load/displacement) and maximum resolved shear stress for each indenter geometry (b).

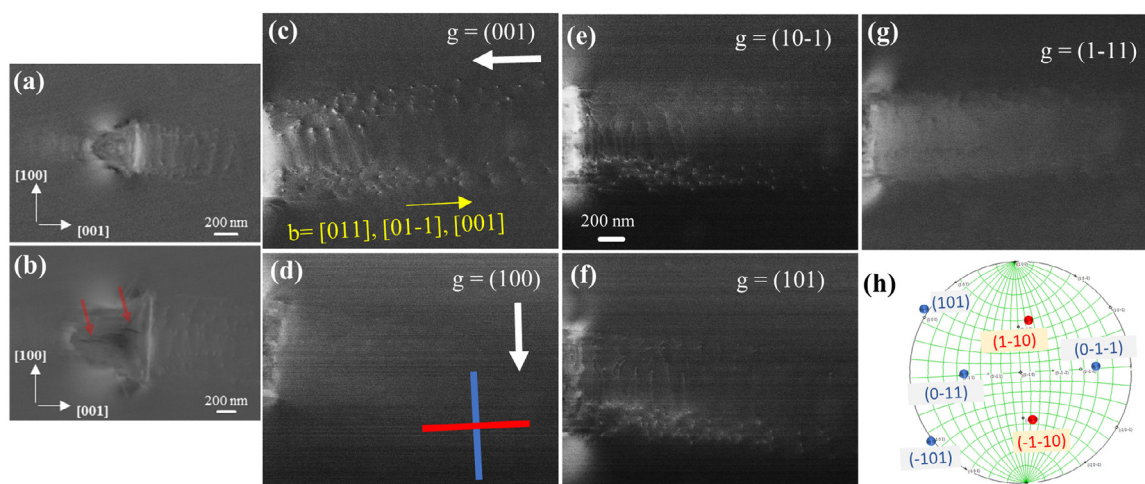


Fig. 3. ECCI micrographs of residual imprints for Berkovich indentation experiments; dislocations are observed in white and black contrast in [001] direction next to the indent. Crack-free indents are obtained in pop-in stop experiments (a), while cracks (red arrows) appear when indentation proceeds to higher loads (b). Dislocation array observed by controlled-ECCI under different channeling conditions (c)–(g). The Burgers vectors [01-1], [011] and [001] have the same projected direction, as marked by the yellow arrow image (c), and can be visualised using the stereographic projection of the crystal (h). Possible pyramidal slip plane traces (0-11) and (0-1-1) are shown by the thick blue line, and the prismatic plane traces (1-10) and (110) are shown by the thick red line. The dislocation line can be seen in image (c). The dislocation lines are perpendicular to the possible Burgers vector and therefore are edge type.

well with reported literature values [14], as determined by KOH etching (see Supplementary Material).

To study the contribution of indentation-induced dislocations to the electrical conductivity, an array of 5×5 indents was created with the pop-in stop technique (Fig. 4b). Here only spherical indentation was performed, using the same indentation parameters as previously described. The distance between indents was kept intentionally small ($1 \mu\text{m}$) in each direction; the dense array aims to create a significant dislocation density within a confined and overlapping plastic zone. Despite overlapping plastic zones ($1.2 \mu\text{m}$) in the indentation array, no surface cracks were observed using SEM imaging. Then, $2 \mu\text{m}$ diameter tungsten (W) electrical contacts were deposited using a focused ion beam (FIB) assisted gas injection system (GIS) in the SEM (Zeiss Auriga), utilizing a 50 pA FIB current for 90 s. The configuration of the contacts consisted of two microcontacts on the top surface separated almost 50 times the contact radius, where the electrical current may flow between contacts [38]. It has been shown that 75% of the voltage drops within a hemisphere of radius four-times the radius of the contact [39]. This means that probing the microcontacts predominately provides insights from the local area. Multiple terminal microcontacts were deposited on (i) the non-deformed (pristine) area, (ii)

an area covering 4 indents, and (iii) an area covering two indents; the specific locations are marked in Fig. 4b. In addition, a reference electrode with commensurate dimensions was deposited $>100 \mu\text{m}$ from the area of interest [38].

Electrical conductivity σ was measured by SEM-supported microcontact impedance spectroscopy. The TiO_2 sample was adhered to a standard SEM stub with conductive silver paint, mounted on a micromanipulator stage (Kleindiek - PS4) and inserted into the SEM chamber (Zeiss Gemini). Tungsten needles with 150 nm tip radii positioned by a micromanipulator were employed, while the bottom side of the sample and SEM stage are grounded. The impedance measurement configuration is schematically illustrated in Fig. 4a and as observed by SEM in Fig. 4c.

In situ SEM impedance spectroscopy (utilizing Hioki IM5355-01 impedance analyser) data was acquired using a voltage amplitude of 1 V in the frequency range of 1 Hz–200 kHz. Three different microelectrodes were inspected for each mechanical state, while each measurement was repeated twice to confirm the reproducibility. The different contacts in each case yielded reproducible Nyquist plots with negligible scatter, and as such, only one data set for each case is presented in Fig. 4d. The bulk semi-circles appear at frequencies ~ 2 kHz up to the highest measured frequency, indicating

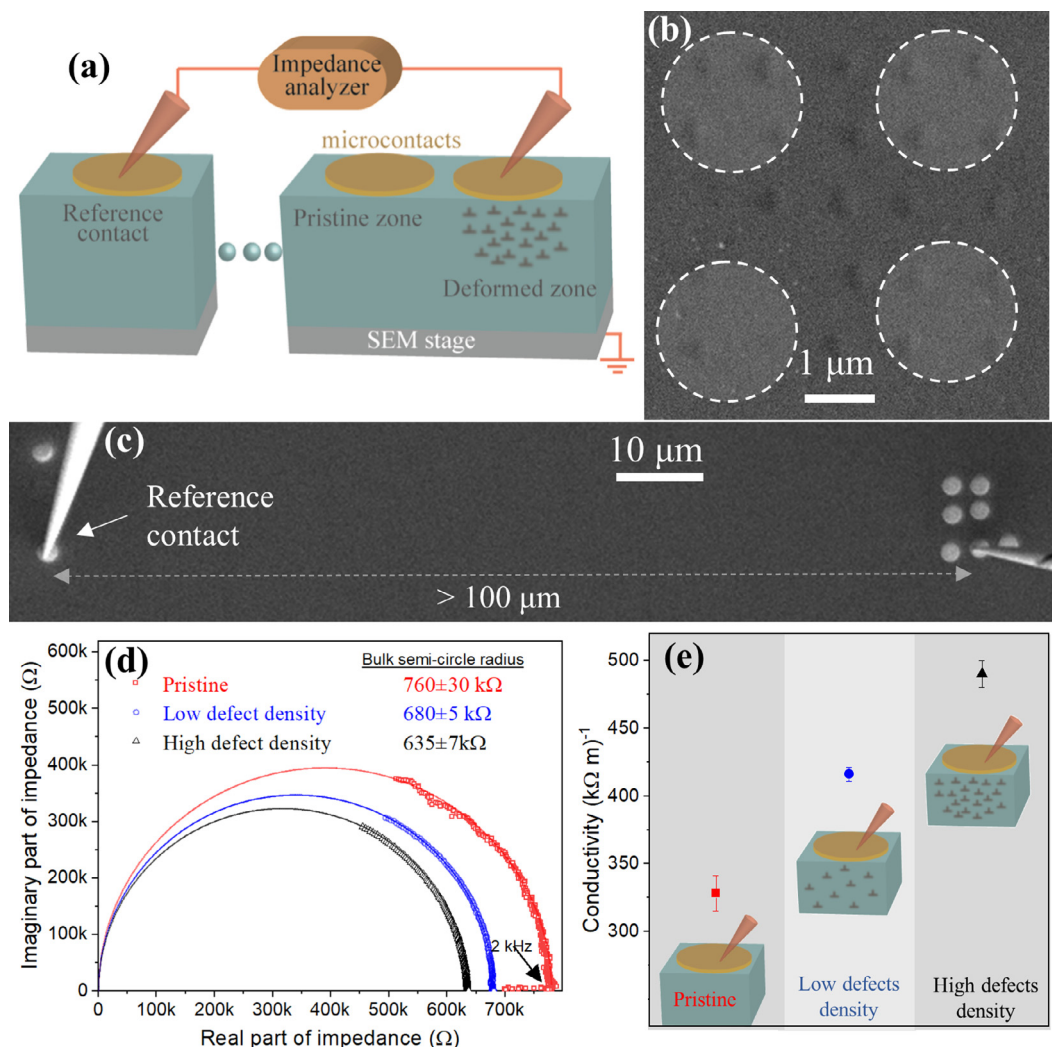


Fig. 4. (a) Schematic illustration of the electrical measurements on indents. Microelectrodes are accessed with a conductive tip driven by a micromanipulator inside the SEM. Impedance spectroscopy is performed between the microelectrodes on the top sample surface (a). An array of shallow indents was created to inspect the conductivity of the deformed area. Regions indicated with the white dashed lines show where microcontacts were deposited (b). A micromanipulator-driven needle probes the microcontact to perform the electrical measurement (c). Representative Nyquist plots of pristine and deformed areas (d); conductivity increase up to ~50% on deformed compared to non-deformed areas for all inspected contacts (e).

a negligible electrode effect. The single semi-circle behavior, consistent for both pristine and deformed material, indicates a dominating bulk response in the measured frequencies [5,15,40]. This implies that localised dislocations enhance the conductivity but the overall electrical behavior is mediated by the bulk or at least by parts of it [15]. Therefore, a series response of the bulk was present while the dislocations themselves are highly conductive. It must be noted that the low frequency data points, observed for the pristine contacts as a 'tail' in the Nyquist plot, exhibit a damping electrical behavior. This low frequency electron degradation occurs when the sample/microelectrode interface dominates the charge transfer, and vanishes when dislocations are introduced to the surface due to an enhanced surface conductivity.

The semi-circular appearance of the data corresponds to bulk conductivity, as confirmed by capacitance values of ~1 pF in this frequency domain [41]. The dislocations presence in the near surface region only slightly reduces capacitance from 0.97 pF in the pristine material and 0.78 pF in the deformed area. This difference in capacitance is not drastic when compared the same type of dislocations formed by bulk compression [5,15], due to the relatively small deformed volume in nanoindentation compared to the extended percolating dislocations in the bulk compression exper-

iments, which implies that capacitance is also influenced by the bulk properties. An ohmic contact is confirmed by the voltage-independent (over 0.5–3 V) resistance of both deformed and pristine areas (not presented here).

From the plot in Fig. 4d the resistances of pristine and deformed areas with a low and high density of defects were determined as 760 ± 30 , 680 ± 5 and 635 ± 7 kΩ, respectively. The error in resistance is determined based on the deviation of the values between multiple contacts combined with the error from the fitting parameter for each experiment. Two data sets of the Nyquist plots for each mechanical state are presented in the Supplementary Material.

The apparent electrical conductivity σ beneath the terminal electrode with radius d is calculated by the equation:

$$\sigma = \frac{1}{2d(2R - R_{pristine})} \quad (2)$$

where R and $R_{pristine}$ are measured resistances for the given microelectrode and pristine area, respectively. The development of Eq. (2) is shown in the Supplementary Material. Therefore, the indents beneath the microcontact caused a conductivity increase from 328 (kΩ m)⁻¹ in the non-deformed area to 416 and 490 (kΩ

m)⁻¹ for low and high densities of defects, respectively, with an error up to 4%. The conductivity data presented in Fig. 4e shows a pronounced conductivity increase up to 50%, which is attributed to the highly conductive dislocations formed by nanoindentation. σ is defined as apparent conductivity since d in Eq. (2) might be larger than the real contact radius when the highly conductive dislocations are present below and next to the electrode. The enhanced electrical conductivity is attributed to the conductive $\langle 011 \rangle$ edge dislocations, consistent with literature interpretation on the bulk-scale [5,15]. Moreover, the high fraction of dislocations are spaced less than 60 nm apart (shown in the Supplemental Material, following analysis in Ref. [42]) – which is less than the estimated space charge affected zone [5]. This might lead to an overlap of the space charge zones of neighbor dislocation lines which consequently contributes a further conductivity increase, in accordance with literature [5,15].

In conclusion, incipient plastic deformation induced by nanoindentation pop-in stop testing, and its impact on the local electrical conductivity, was investigated for rutile TiO₂. The crack-free mechanical deformation at room temperature was precisely controlled using small-radius indenter tips and unloading after the first pop-in caused by $\langle 011 \rangle$ edge dislocations bursts. Using SEM assisted impedance spectroscopy at tungsten microcontacts, a ~50% increase in conductivity was achieved by only a small number of shallow nanoindents arranged in an array. This work of using nanomechanical doping by creating surface dislocations in crack-free volumes is expected to open new opportunities and inspire further research into the local submicron-scale conductivity modification of oxide surfaces using, e.g., large-scale nanoprinting technique, while maintaining material integrity.

Declaration of Competing Interest

The authors declare that they have no known competing financial interests or personal relationships that could have appeared to influence the work reported in this paper.

Acknowledgment

H. B. and G. D. acknowledge the financial support by the ERC Advanced Grant GB CORRELATE (Grant Agreement 787446 GB-CORRELATE). H. T. acknowledges Ph.D. fellowship from the International Max Planck Research School for Surface and Interface Engineering (IMPRS-SurMat). S.N. acknowledges the valuable discussion with Dr. Stefan Zaeferrer and the algorithm search assistance by Mr Manuel Gathmann. Q. K. M. acknowledges funding from the Deutscher Akademischer Austauschdienst (DAAD) for the Ph.D. fellowship with award number 91669061. X. F. acknowledges the support of the Athene Young Investigator Programme (TU Darmstadt).

Supplementary materials

Supplementary material associated with this article can be found, in the online version, at doi:10.1016/j.scriptamat.2022.114543.

References

- [1] A. Nakamura, K. Matsunaga, J. Tohma, T. Yamamoto, Y. Ikuhara, *Nat. Mater.* 2 (2003) 453–456.
- [2] L. Porz, T. Frömling, A. Nakamura, N. Li, R. Maruyama, K. Matsunaga, P. Gao, H. Simons, C. Dietz, M. Rohnke, J. Janek, J. Rödel, *ACS Nano* 15 (6) (2021) 9355–9367.
- [3] K.K. Adepilli, M. Kelsch, R. Merkle, J. Maier, *Adv. Funct. Mater.* 23 (2013) 1798–1806.
- [4] K.K. Adepilli, M. Kelsch, R. Merkle, J. Maier, *Phys. Chem. Chem. Phys.* 16 (2014) 4942–4951.
- [5] Q.K. Muhammad, L. Porz, A. Nakamura, K. Matsunaga, M. Rohnke, J. Janek, J. Rödel, T. Frömling, *Nano Energy* 85 (2021) 105944.
- [6] Y. Ikuhara, *Prog. Mater. Sci.* 54 (2009) 770–791.
- [7] K. Otsuka, A. Kuwabara, A. Nakamura, T. Yamamoto, K. Matsunaga, Y. Ikuhara, *Appl. Phys. Lett.* 82 (2003) 877–879.
- [8] M.D. Armstrong, K.W. Lan, Y. Guo, N.H. Perry, *ACS Nano* 15 (2021) 9211–9221.
- [9] M.K. Nowotny, L.R. Sheppard, T. Bak, J. Nowotny, *J. Phys. Chem. C* 112 (2008) 5275–5300.
- [10] M. Pfanzelt, P. Kubiak, M. Fleischhammer, M. Wohlfahrt-Mehrens, *J. Power Sources* 196 (2011) 6815–6821.
- [11] J. Li, J. Cho, J. Ding, H. Charalambous, S. Xue, H. Wang, X.L. Phuah, J. Jian, X. Wang, C. Ophus, T. Tsakalakos, R.E. Garcia, A.K. Mukherjee, N. Bernstein, C.S. Hellberg, H. Wang, X. Zhang, *Sci. Adv.* 5 (2019) eaaw5519.
- [12] R. Sun, Z. Wang, N. Shibata, Y. Ikuhara, *RSC Adv.* 5 (2015) 18506–18510.
- [13] C. Rodenbücher, G. Bihlmayer, W. Speier, J. Kubacki, M. Wojtyniak, M. Rogala, D. Wrana, F. Krok, K. Szot, *Nanoscale* 10 (2018) 11498–11505.
- [14] K. Szot, G. Bihlmayer, W. Speier, *Solid State Phys.* 65 (2014) 353–559, doi:10.1016/B978-0-12-800175-2.00004-2.
- [15] Q.K. Muhammad, H. Bishara, L. Porz, C. Dietz, M. Ghidelli, G. Dehm, T. Frömling, *Mater. Today Nano* 17 (2022) 100171.
- [16] K.H.G. Ashbee, R.E. Smallman, G.V. Raynor, *Proc. R. Soc. Lond. Ser. A Math. Phys. Sci.* 274 (1963) 195–205.
- [17] K.H.G. Ashbee, R.E. Smallman, G.K. Williamson, *Proc. R. Soc. Lond. A Math. Phys. Sci.* 276 (1963) 542–552.
- [18] K.H.G. Ashbee, R.E. Smallman, *J. Am. Ceram. Soc.* 46 (1963) 211–214.
- [19] S. Takeuchi, T. Hashimoto, *J. Mater. Sci.* 25 (1990) 417–423.
- [20] K. Suzuki, M. Ichihara, S. Takeuchi, *Philos. Mag. A* 63 (1991) 657–665.
- [21] W.M. Hirthe, J.O. Brittain, *J. Am. Ceram. Soc.* 45 (1962) 546–554.
- [22] K.H.G. Ashbee, R.E. Smallman, *Phys. Status Solidi* 4 (1964) 289–298.
- [23] S. Basu, O.A. Elshrief, R. Coward, B. Anasori, M.W. Barsoum, *J. Mater. Res.* 27 (2012) 53–63.
- [24] I. Fernández, A. Cremades, J. Piqueras, *Semicond. Sci. Technol.* 20 (2005) 239–243.
- [25] K. Kurosaki, D. Setoyama, J. Matsunaga, S. Yamanaka, *J. Alloy. Compd.* 386 (2005) 261–264.
- [26] V. Navarro, O. Rodríguez de la Fuente, A. Mascaraque, J.M. Rojo, *Phys. Rev. B* 78 (2008) 224107.
- [27] O.R. de la Fuente, M.A. González-Barrio, V. Navarro, B.M. Pabón, I. Palacio, A. Mascaraque, *J. Phys. Condens. Matter* 25 (2013) 484008.
- [28] X. Fang, K. Ding, S. Janocha, C. Minnert, W. Rheinheimer, T. Frömling, K. Durst, A. Nakamura, J. Rödel, *Scr. Mater.* 188 (2020) 228–232.
- [29] Y. Gaillard, C. Tromas, J. Woïrgard, *Acta Mater.* 54 (2006) 1409–1417.
- [30] D. Lorenz, A. Zeckzer, U. Hilpert, P. Grau, H. Johansen, H.S. Leipner, *Phys. Rev. B* 67 (2003) 172101.
- [31] T.F. Page, W.C. Oliver, C.J. McHargue, *J. Mater. Res.* 7 (1992) 450–473.
- [32] X. Fang, H. Bishara, K. Ding, H. Tsybenko, L. Porz, M. Höfling, E. Bruder, Y. Li, G. Dehm, K. Durst, *J. Am. Ceram. Soc.* (2021) n/a.
- [33] H. Li, R.C. Bradt, *J. Mater. Sci.* 28 (1993) 917–926.
- [34] K.L. Johnson, in: *Contact Mechanics*, Cambridge University Press, Cambridge, 1985, pp. 84–106.
- [35] X. Fang, L. Porz, K. Ding, A. Nakamura, *Crystals* 10 (10) (2020) 933.
- [36] J.R. Morris, H. Bei, G.M. Pharr, E.P. George, *Phys. Rev. Lett.* 106 (2011) 165502.
- [37] S. Pathak, D. Stojakovic, R. Doherty, S.R. Kalidindi, *J. Mater. Res.* 24 (2009) 1142–1155.
- [38] R.A. Veazey, A.S. Gandy, D.C. Sinclair, J.S. Dean, *J. Am. Ceram. Soc.* 102 (2019) 3609–3622.
- [39] J. Fleig, *Solid State Ion.* 161 (2003) 279–289.
- [40] K. Otsuka, K. Matsunaga, A. Nakamura, S. Ii, A. Kuwabara, T. Yamamoto, Y. Ikuhara, *Mater. Trans.* 45 (2004) 2042–2047.
- [41] J.T.S. Irvine, D.C. Sinclair, A.R. West, *Adv. Mater.* 2 (1990) 132–138.
- [42] M. Haeri, M. Haeri, *J. Open Res. Softw.* 3 (2015) 1.